Electronic and optical properties of ferromagnetic Ga$_{1-x}$Mn$_x$As in a multiband tight-binding approach

Marko Turek,[*] Jens Siewert, and Jaroslav Fabian

Institut für Theoretische Physik, Universität Regensburg, D-93040 Regensburg, Germany
(Received 23 May 2008; revised manuscript received 17 July 2008; published 15 August 2008)

We consider the electronic properties of ferromagnetic bulk Ga$_{1-x}$Mn$_x$As at zero temperature using two realistic tight-binding models, one due to Tang and Flatté and one due to Mašek. In particular, we study the density of states, the Fermi energy, the inverse participation ratio, and the optical conductivity with varying impurity concentration $x = 0.01-0.15$. The results are very sensitive to the assumptions made for the on-site and hopping matrix elements of the Mn impurities. For low concentrations, $x < 0.02$, Mašek's model shows only small deviations from the case of p-doped GaAs with increased number of holes while within Tang and Flatté's model an impurity-band forms. For higher concentrations x, Mašek's model shows minor quantitative changes in the properties we studied while the results of the Tang and Flatté model exhibit qualitative changes including strong localization of eigenstates with energies close to the band edge. These differences between the two approaches are in particular visible in the optical conductivity, where Mašek's model shows a Drude peak at zero frequency while no such peak is observed in Tang and Flatté's model. Interestingly, although the two models differ qualitatively the calculated effective optical masses of both models are similar within the range of 0.4–1.0 of the free-electron mass.

PACS number(s): 75.50.Pp, 71.55.Eq, 72.80.Ey, 75.50.Dd

I. INTRODUCTION

Dilute magnetic semiconductors are investigated very actively for their potential of combining ferromagnetic with semiconducting properties. A prominent prototype is Ga$_{1-x}$Mn$_x$As with Mn concentrations being typically $x = 0.01-0.15$.[1–4] For these intermediate to large concentrations critical temperatures up to 170 K could be observed.[5] The host material, GaAs, is a III–V semiconductor with a band gap of 1.5 eV. When the Mn impurities substitute the Ga atoms, they act as acceptors which carry a local magnetic moment caused by the half-filled d-shell. This leads to a hole-mediated ferromagnetism.[6] The impurity binding energy is 0.11 eV.[7] If the Mn concentration exceeds a critical value $x \approx 0.01$, the impurity wave functions at the Fermi energy overlap sufficiently for the material to undergo a transition toward a metallic state.

A widely discussed question is whether the holes reside in an impurity band which is detached from the host valence band or in the valence band itself, which would cause different transport properties.[4] To this end a variety of absorption experiments[8–11] and measurements of the band gap and chemical potential[12,13] in GaMnAs were performed. For very low concentrations $x \ll 0.01$, an impurity band is formed with the Fermi energy residing therein.[14] This picture has also been used for the intermediate concentration range, $x \approx 0.01-0.15$, to explain optical measurements.[8] On the other hand, there is experimental indication that the impurity band and the valence band have completely merged, see Ref. 14 and references therein. Another issue concerns the localization properties of the carriers. It has been argued that instead of the impurity-band interpretation the assumption of a merged valence and impurity band together with the existence of localized states in the band tail can explain the experiments.[14]

Besides the experimental efforts for a better understanding of the electronic properties of Ga$_{1-x}$Mn$_x$As, a wide range of theoretical models has been developed.[2] Among these are first-principles calculations,[15,16] effective single-particle tight-binding approaches,[17–20] tight-binding approaches in combination with percolation theory,[21–23] dynamical mean-field theories,[24] effective theories based on $k \cdot p$ Hamiltonians,[25–28] and large-scale Monte Carlo studies of a real space Hamiltonian.[29] The microscopic tight-binding approach has the advantage that one can study disordered systems in a nonperturbative way. The basis for this approach is the $16 sp^3$ valence and conduction bands of GaAs that are approximated very closely to experimental data throughout the entire Brillouin zone. System sizes up to approximately 2000 atoms can be treated within this approach with reasonable numerical effort.

In this paper we present our results concerning the electronic structure of bulk Ga$_{1-x}$Mn$_x$As at zero temperature. We assume the system to be ferromagnetic by aligning all Mn core spins into the z direction. Specifically, we focus on the role of substitutional Mn impurities by neglecting interstitial disorder. The basis for our studies are well-known sp^3 tight-binding models for the host material GaAs which include spin-orbit coupling.[30,31] The disorder effects are treated in a nonperturbative way by changing the on-site and hopping terms of those Ga sites that are replaced by the Mn impurities. Instead of describing the effects of the Mn impurities by the two sp-d exchange constants $N_0\alpha$ and $N_0\beta$ only,[18,19] we follow two more elaborate approaches. The first approach, by Mašek[20,32] (referred to as model A), uses first-principles methods to determine the tight-binding parameters of the Mn impurities in a concentration regime around 10%. The second approach, by Tang and Flatté[17,33] (model B), is based on a fit of the physically relevant tight-binding parameters to reproduce the binding energy of a single Mn impurity in the host material. Both approaches result in effective single-particle tight-binding models in which the carrier-carrier correlations are included in a mean-field way. This approxima-

tion is justified in the intermediate to high doping regime, i.e., $x \gtrsim 0.01$.[14] Nevertheless, explicit inclusion of carrier-carrier interactions could lead to quantitative corrections which enhance localization effects.[34]

In Sec. II we summarize the two approaches of how to find the reliable parameter sets for the inclusion of the Mn impurities and introduce our numerical method for solving the resulting equations in more detail. The explicit calculation of the eigenenergies and eigenstates allows us to investigate the density of states and the position of the Fermi energy. In Sec. III we show that for Mašek's model (*A*) the valence band is only slightly deformed while for the model by Tang and Flatté (*B*) an impurity-band forms which starts to merge with the host valence band at $x \approx 0.01$. The spatial extension of the states around the Fermi energy is investigated in Sec. VI by means of the inverse participation ratio. We show that the states related to the impurity band show strong localization when their energy is close to the band edge. Based on the spectrum and the eigenfunctions, we calculate the experimentally relevant optical conductivity. The relation of these results to the experimental findings is discussed in Sec. V.

II. TIGHT-BINDING APPROACH

Our analysis within the framework of a phenomenological tight-binding approach[35,36] is based on an effective single particle Hamiltonian allowing for material-specific simulations of bulk GaMnAs systems. We considered disordered supercells of up to 2000 atoms with the supercell size being limited by the available computer resources only. In this work we focus on substitutional disorder by changing the on-site and hopping terms of certain Ga sites which are replaced by Mn.

In order to introduce the terminology we briefly summarize the tight-binding approach. Using the single-particle basis,

$$\chi_{\vec{k}oa}(\vec{r}) = \frac{1}{\sqrt{S}} \sum_{\vec{R}} \exp[i\vec{k}(\vec{R} + \vec{t}_a)]\phi_o(\vec{r} - \vec{t}_a - \vec{R}), \qquad (1)$$

the eigenstates of the Hamiltonian can be written as

$$\Psi_{\vec{k}}^{(b)}(\vec{r}) = \sum_{o,a} c_{\vec{k}oa}^{(b)}\chi_{\vec{k}oa}(\vec{r}). \qquad (2)$$

Here, o labels the atomic orbital ϕ_o, a specifies the atom sitting at the position $\vec{t}_a$ within the supercell, S is the total number of supercells and $\vec{R}$ points to the several supercells that are included. The sum over o and a in Eq. (2) thus runs over all orbitals of all N atoms in a supercell. Due to the periodicity and the Bloch character of the basis states $\chi_{\vec{k}oa}$, the Hamiltonian is block diagonal with respect to the different $\vec{k}$ vectors. The matrix elements in this basis thus read

$$[H(\vec{k})]_{oa,o'a'} = \sum_{\Delta\vec{R}_{nn}} \exp(i\vec{k}\vec{r}_{nn})\langle\phi_{oa}(\vec{r})|H|\phi_{o'a'}(\vec{r} - \vec{r}_{nn})\rangle,$$

$$(3)$$

where the sum goes over all the supercells that contain the nearest or next to nearest neighbors, depending on the ap-

proximation employed. The vector $\vec{r}_{nn}$ points from atom a to atom a' so that $\vec{r}_{nn} = \Delta\vec{R}_{nn} + \vec{t}_{a'} - \vec{t}_a$. On-site terms are thus characterized by $\vec{r}_{nn} = 0$ while hopping terms correspond to $\vec{r}_{nn} \neq 0$. Numerical diagonalization of the matrix [Eq. (3)] returns the eigenenergies and the eigenvectors as a linear combination of the localized atomic orbitals $\phi_{oa}(\vec{r})$.

We have studied two different parameter sets for the inclusion of Mn impurities into existing tight-binding models for GaAs. The first set due to Mašek (model *A*) is derived from a first-principles approach while the second one due to Tang and Flatté (model *B*) is based on phenomenologically deduced parameters. In either case we checked our simulation by first calculating the band structure and density of states for clean GaAs using the tetrahedron method.[37] Then we considered disordered supercells which are repeated periodically, and their ensembles. The sizes of the supercells are typically between 128 and 1024 atomic sites while the disorder averages were performed over 5–15 random configurations, depending on the system size and the number of impurities. The finiteness of the systems limits the impurity concentrations to $x \gtrsim 0.006$. As we will demonstrate below, the density of states is self-averaging for supercells of the above-mentioned sizes so that increasing the number of disorder averages decreases the fluctuations of the results but does not give any new qualitative features. The self-averaging property also allows to imply periodic boundary conditions to the supercells by which less fluctuating results can be obtained. These periodic repetitions of the supercells correspond to a summation over various $\vec{k}$ points in the Brillouin zone. In our calculations we used between 20 and 505 different points in $\vec{k}$ space which are chosen in close resemblance to the ones given by the tetrahedron method. However, in contrast to the clean system, a linear interpolation of the band structure does not give an improvement of the quality of the results as the eigenenergies of a disordered supercell for a given $\vec{k}$ lie too close to each other.

1. Model A (Mašek)

The first model we study was introduced by Mašek.[20] It starts from a tight-binding approach for the host material which includes the first and second-nearest-neighbor interactions[31] as well as spin-orbit coupling.[30] This gives a rather accurate description of the band structure including the conduction bands away from the Γ point. The on-site and hopping terms for the Mn impurity in the disordered system were obtained from a first-principles calculation using a self-consistent Hartree-Fock approximation for a single Mn impurity hybridized in a GaAs lattice.[20,32] The energy shift of the s states is assumed to be proportional to the difference of calculated atomic levels while the on-site energies of the p states remain unchanged. This procedure gives for the on-site energies $E_{\text{Mn},s\uparrow} = -0.4$ eV, $E_{\text{Mn},s\downarrow} = 0.0$ eV, and $E_{\text{Mn},p} = 4.374$ eV. Additionally, the ten d orbitals of Mn are explicitly included. These orbitals can be divided into two subgroups according to their symmetry, i.e., $(\text{Mn}, t2)$ and (Mn, e). The corresponding values are $E_{\text{Mn},t2\uparrow} = -2.21981$ eV, $E_{\text{Mn},t2\downarrow} = 2.63427$ eV, $E_{\text{Mn},e\uparrow} = -3.01348$ eV, and $E_{\text{Mn},e\downarrow} = 2.36445$ eV. Finally, it was

assumed that the Mn d states hybridize only with the s and p orbitals of the nearest neighbors. The relevant hopping parameters based on the Harrison rules[32,36] are $V_{sd,\sigma}$ $=-1.1077$ eV, $V_{pd,\sigma}=-1.0341$ eV, and $V_{pd,\pi}=0.4767$ eV. These resulting parameters were then checked within the same theoretical framework for a system with 10% of the Ga atoms replaced by Mn and appeared to be robust. The model is supported by photoemission spectroscopy experiments[38] that revealed only minor differences in the band structure of $Ga_{1-x}Mn_xAs$ compared to GaAs except for the appearance of the additional Mn d states.

2. Model B (Tang, Flatté)

The second model we studied was introduced by Tang and Flatté.[17,33] The electronic structure of the GaAs host material is described by a slightly different sp^3 tight-binding model which also includes spin-orbit coupling but remains within the nearest-neighbor approximation.[30] Despite the lack of the second-nearest-neighbor terms this model gives a fairly accurate description of the band structure of GaAs around the Γ point. The replacement of a Ga atom by a Mn impurity is modeled by an effective potential which describes the changes in on-site energies and hybridization of the Mn d-orbitals with the As p-orbitals. The Mn d-orbitals are not part of the basis set of atomic orbitals as they are included indirectly by a spin-dependent effective energy shift of the nearest-neighbor p orbitals. There are two independent parameters of the effective impurity potential. They are given by compensating the difference in the atomic ionization energies and by fitting the experimentally[7] obtained Mn acceptor level lying at 0.11 eV. This fitting procedure is based on the Koster-Slater technique to calculate the host Green's function and the subsequent inclusion of the impurity potential via Dyson's equation for studying the local density of states. From the resulting parameters the corresponding p-d exchange interaction can be estimated to be ≈-0.3 eV while the experimental value was found to be ≈-1.2 eV.[17,39] The model was applied to describe single Mn atoms and Mn pairs in GaAs and showed good agreement with experimental results for the local and total density of states as well as the shape of the wave functions.[33] This apparently good description of Mn pairs is the main motivation to apply the model to diluted disordered bulk systems and study its applicability in the regime of highly doped magnetic semiconductors.

III. DENSITY OF STATES

The density of states, $d(E,x,N)$, is obtained by direct diagonalization of the tight-binding Hamiltonian (3) and the evaluation of the sum

$$d(E,x,N) = \frac{1}{n(\infty)} \sum_{b,\vec{k}} \delta_\epsilon(E - E_{\vec{k}}^{(b)}),\qquad(4)$$

where $\delta_\epsilon(E)$ is a broadened delta function of the chosen width $\epsilon=5$ meV. The eigenvalues $E_{\vec{k}}^{(b)}$ of the Hamiltonian are labeled by the band index b. The density of states is normalized by the total number of states $n(\infty)$. As the parameter sets for clean GaAs are different for the two models, the
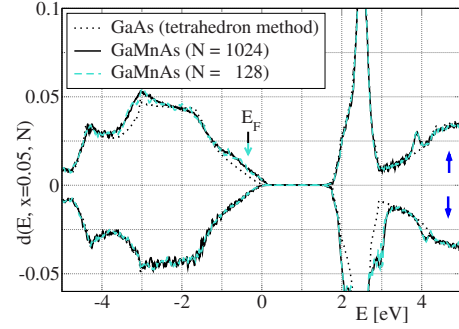

FIG. 1. (Color online) Model A: Density of states for clean GaAs (black dotted, tetrahedron method) and disordered GaMnAs. The Mn concentration is $x=0.05$. System sizes are $N=128$ sites (505 $\vec{k}$ vectors, 15 disorder configurations) and $N=1024$ sites (20 $\vec{k}$ vectors, 5 disorder configurations). The arrow indicates the position of the Fermi energy, $E_F=-0.34$ eV. The upper (lower) part of the figure shows the spin-up (down) contribution to the density of states.

resulting densities of states also show different behavior, in particular for the conduction band, see Figs. 1 and 2.

The results for a Mn concentration $x=0.05$ and two different system sizes are shown in Figs. 1 and 2 for the models A (Mašek) and B (Tang, Flatté), respectively. In both cases one can clearly observe the self-averaging properties of the density of states—the deviations between the two systems of different sizes are on the same order as the fluctuations due to the disorder. This self-averaging property of the density of states can be observed for the entire range of concentrations studied. This implies that the quantity $d(E,x,N)=d(E,x)$ is independent of the system size N if the smaller fluctuations are neglected.

For model A (Mašek) one finds that the density of states is only slightly perturbed in comparison to the density of states for the clean system. This is in contrast to the results of model B (Tang, Flatté) where, especially around the top of the valence band of the host material, the number of spin-up states is significantly enhanced. In either model the spin-
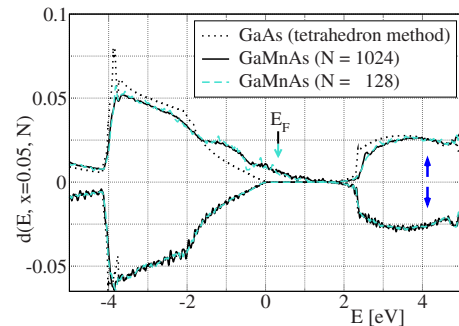

FIG. 2. (Color online) Model B: Density of states for clean GaAs (black dotted, tetrahedron method) and disordered GaMnAs. The Mn concentration is set to $x=0.05$. System sizes are $N=128$ sites (505 $\vec{k}$ vectors, 15 disorder configurations) and $N=1024$ sites (20 $\vec{k}$ vectors, 5 disorder configurations). The arrow indicates the position of the Fermi energy, $E_F=0.30$ eV. The upper (lower) part of the figure shows the spin-up (down) contribution to the density of states.
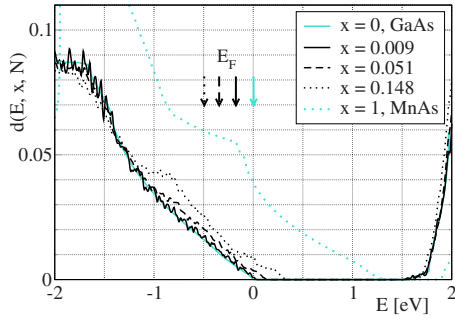
FIG. 3. (Color online) Model *A*: Density of states of GaMnAs. The Mn concentration is set to $x=0.009$ (1024 atoms, $20\vec{k}$ vectors, 5 disorder configurations), $x=0.051$ (432 atoms, $89\vec{k}$ vectors, 10 disorder configurations), and $x=0.148$ (432 atoms, $89\vec{k}$ vectors, 10 disorder configurations). The arrows indicate the positions of the corresponding Fermi energies: $E_F(x=0.009)=-0.17$ eV, $E_F(x=0.051)=-0.34$ eV, $E_F(x=0.148)=-0.49$ eV. For comparison the densities of states for clean GaAs and MnAs are shown.

down contribution of the valence band remains unaltered.

As energies around the Fermi energy are most interesting we present the density of states for a smaller energy window and various Mn concentrations in the Figs. 3 and 4. For model *A* (Mašek), increasing the Mn concentration from 1% to 15% does not change the qualitative but only quantitative characteristics of the density of states. In particular, no detached impurity band forms within this model and the given range of Mn concentrations. The size of the band gap decreases as some of the spin-up states are shifted from below the top of the valence band into the gap of the host material. However, as adding Mn impurities also adds holes, the Fermi energy decreases and moves deeper into the valence band, see also Fig. 5. Thus, the major effect of an increasing number of Mn impurities is the larger number of holes which leads to a lowering of the Fermi energy. This trend qualitatively follows the Fermi energy of pure GaAs with the corresponding number of holes added, see Fig. 6.

For model *B* (Tang, Flatté) a completely different picture arises. Due to the strong effective potential of the Mn impu-
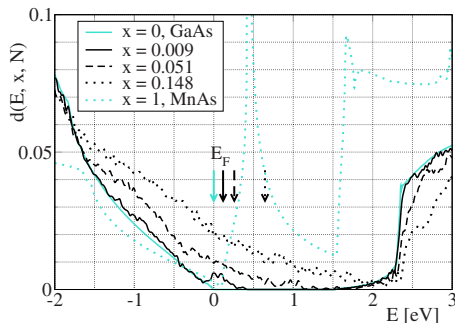

FIG. 4. (Color online) Model *B*: Density of states of GaMnAs. The Mn concentration is set to $x=0.009$ (686 atoms), $x=0.051$ (432 atoms), and $x=0.148$ (432 atoms). In either case 89 $\vec{k}$ vectors and 10 disorder configurations were used. The arrows indicate the positions of the corresponding Fermi energies: $E_F(0.009)=0.10$ eV, $E_F(0.051)=0.30$ eV, $E_F(0.148)=0.65$ eV. For comparison the densities of states for clean GaAs and MnAs are shown.
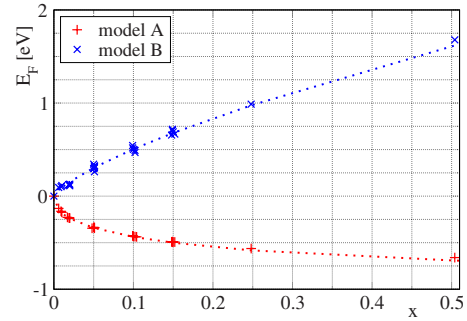

FIG. 5. (Color online) Models *A* and *B*: Fermi energy of GaMnAs as a function of the impurity concentration measured from the top of the *GaAs host* valence band. The Fermi energy of model *A* moves into the host valence band while it increases into the host gap for model *B*. System sizes between 128 and 1024 atoms are shown. The dotted lines serve as a guide to the eye.

rities there is a large number of states shifted from the host valence band far into the gap. Already at concentrations of 5% there is almost no gap left at all. The second effect of the addition of Mn impurities is again the increased number of holes which lowers the Fermi energy. However, for model *B* (Tang, Flatté) this increasing number of holes does not compensate the effect of the large number of states appearing in the host gap. Hence one observes an increasing Fermi energy, measured relative to the top of the host valence band, see Fig. 5. The second major difference to model *A* (Mašek) is the appearance of a detached impurity band for small enough impurity concentrations. This impurity band starts to merge with the valence band for concentrations around 1%, see Fig. 4, which is consistent with experimental data.[40] Its center is positioned at the impurity binding energy of Mn while its half width is on the order of 0.1 eV. For $x \gtrsim 0.05$ one cannot distinguish the impurity band from the valence band anymore as the two bands have merged completely.

The results for the Fermi energy and the band gap are summarized in Figs. 5 and 6. In Fig. 5 the Fermi energy of GaMnAs measured with respect to the top of the *GaAs host* valence band is shown. From the behavior of the Fermi energy as a function of the impurity concentration, it is evident
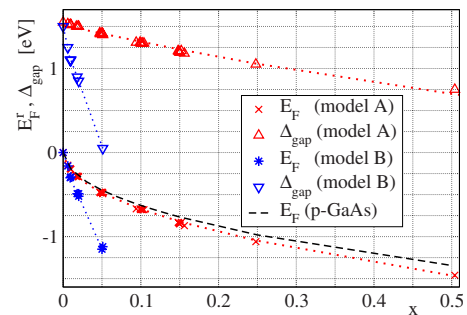

FIG. 6. (Color online) Models A and B: Fermi energy E_F^r measured relative to the top of the *GaMnAs* valence band and gap size Δ_{gap}. The dotted lines serve as a guide to the eye. The dashed line shows the Fermi energy of *p*-GaAs without impurities where the number of holes is adjusted to the corresponding GaMnAs impurity concentration x.

that the two effects of adding holes and shifting states are of unequal importance for the two models, as described in the previous paragraphs. In Fig. 6 we present the Fermi energy measured with respect to the *GaMnAs* valence band. By choosing these concentration dependent reference points for the energy, we partially suppress the effects due to the shifted states. Hence, the Fermi energy decreases with respect to this energy reference point for both models. Again one finds that the addition of the holes is the major effect for model *A* (Mašek) as the resulting Fermi energy behaves very similar to the case of clean *p*-GaAs with the corresponding number of holes added, see Fig. 6. Furthermore we have included the results for the band gap Δ_{gap} into Fig. 6. This information can be used in the design and study of spintronic devices including hole injection into GaMnAs. The stronger influence of the disorder in model *B* (Tang, Flatté) compared to model *A* (Mašek) becomes evident as the size of the gap is much faster decreasing for model *B*. Experiments based on scanning tunneling microscopy conductance spectra resulted in an estimate $\Delta_{gap} \approx 1.23$ eV for $x \approx 0.03$ (Ref. 12) and, more recently, photoconductivity measurements on GaMnAs heterostructures yielded $\Delta_{gap} \approx 1.41$ eV for the same Mn concentration.[13] The chemical potential was found to be in the vincinity of the Mn impuritiy level.[13] However, the considered samples were unannealed or annealed only for short times implying a significantly reduced carrier concentration due to Mn intersticials. Therefore, a direct comparison with our data is not possible and further, more detailed, experimental investigations are necessary in order to decide which model provides a more accurate description.

The differences for the density of states between the two models can be better understood when the density for a clean MnAs ($x=1$) system is calculated. As zinc-blend MnAs does not form a stable configuration[41] this calculation does not correspond to a real physical system. Nevertheless it describes the $x \to 1$ limit of the two models giving a good indication of what to expect for increasing x. The parameterization of model *A* (Mašek) results in an increased number of states for MnAs in the gap of GaAs. For the disordered GaMnAs there is a clear tendency for the density of states to change from the GaAs shape ($x=0$) toward the MnAs shape ($x=1$). This can, for example, be seen by the formation of the shoulder in the density of states at $E \approx -1$ eV and $x=0.148$, see Fig. 3. For model *B* (Tang, Flatté), the MnAs density shows a qualitatively new feature at $E \approx 0.5$ eV in the gap of the GaAs, seen in Fig. 4. The appearing peak is due to the shift in the energies of the *p* states which is reflected in the rapidly vanishing gap for the disordered GaMnAs.

IV. INVERSE PARTICIPATION RATIO

Besides the density of states and the Fermi energy we also studied the character of the eigenstates, in particular, their localization properties. To this end we analyzed the inverse participation ratio averaged over all states in a given energy window:
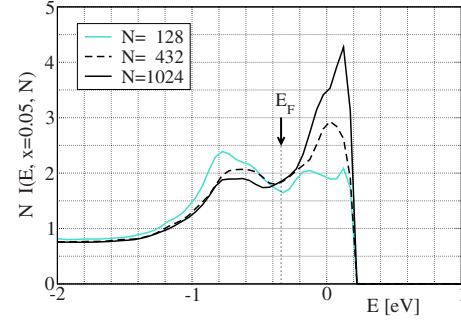

FIG. 7. (Color online) Model *A*: Scaled inverse participation ratio $[N \cdot I(E,x,N)]$ for fixed concentration $x=0.05$ and various system sizes $N=128$ (505$\vec{k}$ vectors, 15 configurations), $N=432$ (89$\vec{k}$ vectors, 10 configurations), and $N=1024$ (20$\vec{k}$ vectors, 5 configurations). The arrow indicates the position of the Fermi energy $E_F = -0.34$ eV.

$$I(E,x,N) = \frac{\sum_{b,\vec{k},a} |\sum_o |c_{\vec{k}oa}|^2|^2 \delta_\epsilon[E - E_{\vec{k}}^{(b)}]}{\sum_{b,\vec{k}} \delta_\epsilon[E - E_{\vec{k}}^{(b)}]}. \quad (5)$$

Qualitatively, the participation ratio corresponds to the average number N_{occ} of sites occupied by the eigenstates of given energy E, i.e., $1/I \sim N_{occ}$. Thus, $I(E,x,N)$ scales with the inverse system size for extended states as the probability $\sum_o |c_{\vec{k}oa}|^2$ to find the electron at a certain atom is on the order of the inverse system size. For strongly localized states $I(E,x,N)$ remains constant independently of the system size.

First, we consider the scaling of $[N \cdot I(E,x,N)]$ with system size N for a fixed impurity concentration. The results for the two models are shown in Figs. 7 and 8 where $[N \cdot I(E,x=0.05,N)]$ is plotted. As expected, one finds extended states for the energies deep within the valence band. As the energy is increased toward the Fermi energy, the value of $[N \cdot I(E,x,N)]$ increases, meaning that on average, less atoms participate in the corresponding states. Comparing Figs. 7 and 8 one finds this effect to be much stronger for model *B* (Tang, Flatté). Nevertheless a clear linear scaling of
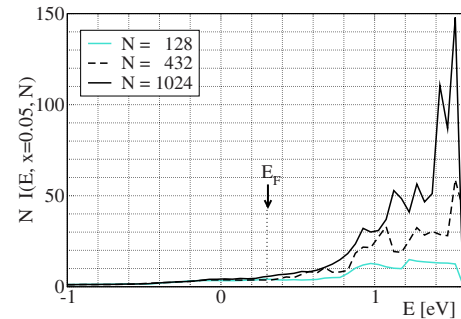

FIG. 8. (Color online) Model *B*: Scaled inverse participation ratio $[N \cdot I(E,x,N)]$ for fixed concentration $x=0.05$ and various system sizes $N=128$ (505$\vec{k}$ vectors, 15 configurations), $N=432$ (89$\vec{k}$ vectors, 10 configurations), and $N=1024$ (20$\vec{k}$ vectors, 5 configurations). The arrow indicates the position of the Fermi energy $E_F = 0.30$ eV.
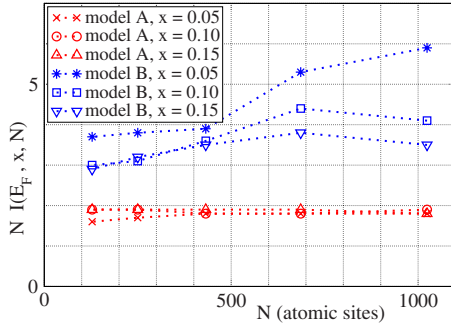
FIG. 9. (Color online) Models A and B: Scaled inverse partici-pation ratio $[N \cdot I(E_F, x, N)]$ at the Fermi energy as a function of the system size N. Mn concentrations $x = 0.05$, 0.10, and 0.15 are shown for models A and B.

$[N \cdot I(E_F, x, N)]$ with system size N, which would indicate strongly localized states at the Fermi energy, cannot be found, see Fig. 9. This implies that the states around the Fermi energy reside on a subset of lattice atoms; yet they are still extended throughout the sample. This holds true for con-centrations between 5% and 15%, see Fig. 9. For model B (Tang, Flatté), this effect is more pronounced and we will argue that the states are spread over the sublattice of Mn sites. As the density of states decreases for energies closer to the band edge there are less states giving a contribution to the inverse participation ratio [Eq. (5)]. This causes the stronger fluctuations in $I(E, x, N)$ that can be observed for energies around and above the Fermi energy.

Going from the Fermi energy E_F to higher energies close to the band edge, E_{be}, the states remain delocalized for model A (Mašek) while they show strong localization for model B (Tang, Flatté). Qualitatively this conclusion is supported by the following argument. If an impurity state is strongly lo-calized it cannot overlap with other impurity states located at neighboring impurity sites. This implies that the number of sites occupied by an impurity state must be significantly smaller than N/N_{Mn}. As the participation ratio is a measure for the number of occupied sites N_{occ} it follows that the states are strongly localized only if $I(E, x, N)$ is large enough so that $x \lesssim I(E, x, N)$ independent of the system size N. This is consistent with the statement that $I(E, x, N)$ scales inversely with the system size N for extended states while it remains constant for localized states. For model A (Mašek) the con-dition $x \lesssim I(E, x, N)$ is never fullfilled in the entire energy range, see Fig. 7. However, for model B (Tang, Flatté), going beyond the Fermi energy this criterion can be fulfilled im-plying that there are localized states, see Fig. 8.

To demonstrate this localization property for model B (Tang, Flatté) in more detail we show the maximum values of $[N \cdot I(E, x, N)]$, which correspond to energies E_{be} close to the band edge, in Fig. 10. The clear linear increase of the scaled inverse participation ratio for the states closer to the band edge indicates strong localization at E around E_{be}. On the other hand, at lower energies $E = E_F + 0.5$ eV, a transition from delocalized to localized states takes place depending on the concentration of Mn impurities, see the inset of Fig. 10. The linear increase of $[N \cdot I(E_F + 0.5 \text{ eV}, x, N)]$ with size N indicates localized states for concentrations $x < 0.15$. On the

other hand, the scaled inverse participation ratio remains constant for $x = 0.15$ for all system sizes meaning that the states are extended. Obviously, the concentration of Mn im-purities is in this case large enough for the impurity states to overlap. Generally one can assume that for each fixed energy E there is a critical concentration $x_{crit}(E)$ for which the slope of $[N \cdot I(E, x, N)]$ vanishes. Based on this critical concentra-tion, one can estimate the spatial extension of the Mn impu-rity states. The average distance of impurities for given con-centration x is approximately 0.4 nm $\cdot x^{-1/3}$. For the critical concentration $x_{crit}(E)$ the impurity states start to overlap as the transition from localization to delocalization takes place. Therefore the spatial extension of the states at a fixed energy can be estimated by 0.4 nm $\cdot x_{crit}^{-1/3}(E)$. From Fig. 8 we find $x_{crit}(E_F + 0.5 \text{ eV}) \approx 0.15$ implying that the impurity states ex-tend over a range of ≈ 0.7 nm. At higher energies, E_{be}, ex-trapolation of our data leads to $x_{crit}(E_{be}) \approx 0.18$ and a spatial extension of the impurity states of ≈ 0.6 nm. This estimate is consistent with the experimentally deduced value.[10]

In a second step we analyze the influence of the Mn con-centration on the inverse participation ratio (5). Figures 11 and 12 show the results for a fixed system size $N = 432$ for models A (Mašek) and B (Tang, Flatté), respectively. For comparison, we have also included the result of a larger sys-tem with a smaller concentration of Mn impurities. In the
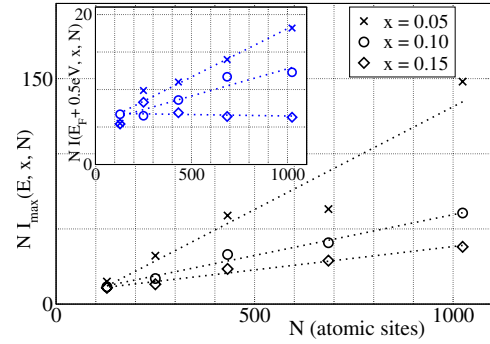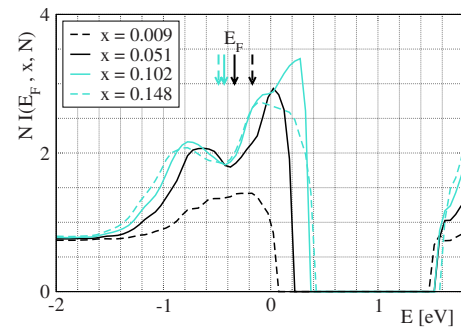

FIG. 10. (Color online) Model B: Maximum value of the scaled inverse participation ratio $[N \cdot I_{max}(E_{be}, x, N)]$ for energies close to the valence-band edge as a function of the system size N. The inset shows the same quantity at energies $E_F + 0.5$ eV.

FIG. 11. (Color online) Model A: Scaled inverse participation ratio $[N \cdot I(E, x, N)]$ for various concentrations $x = 0.009$ (1024 at-oms, $20\vec{k}$ vectors, 5 disorder configurations), $x = 0.051$, 0.102, and 0.148 (432 atoms, $89\vec{k}$ vectors, 10 disorder configurations). The arrows indicate the positions of the Fermi energy.

FIG. 12. (Color online) Model B: Scaled inverse participation ratio $[N \cdot I(E,x,N)]$ for various concentrations $x=0.009$ (1024 atoms, $20\vec{k}$ vectors, 5 disorder configurations), $x=0.051$, 0.102, and 0.148 (432 atoms, $89\vec{k}$ vectors, 10 disorder configurations). The arrows indicate the positions of the Fermi energy.
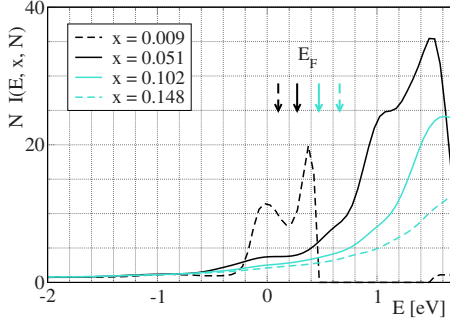
case of model A (Mašek), the increase of $[N \cdot I(E,x,N)]$ with increasing energy starts first for the highest concentration $x=0.15$. The reason can be found in the density of states—the larger x is, the stronger the valence band changes. However, if one considers $[N \cdot I(E_\mathrm{F},x,N)]$ at the Fermi energy, which also depends on x, the influence of the concentration is negligible, see Fig. 13, where $1/[N \cdot I(E_\mathrm{F},x,N)]$ is plotted as a function of x.

For model B (Tang, Flatté) the situation is different since $[N \cdot I(E_\mathrm{F},x,N)]$ increases with decreasing concentration x, as shown in Fig. 12, meaning that the number of occupied sites increases with x. This suggests that the states around the Fermi energy tend to the Mn sublattice. This interpretation is supported by the fact that $1/[N \cdot I(E_f,x,N)]$ increases linearly with the concentration x, see Fig. 13. As $1/[N \cdot I(E_f,x,N)]$ is a measure for the relative number of atoms where the states reside, one can conclude that for model B (Tang, Flatté) the states tend to spread on the Mn sublattice and nearby sites. As an independent check of this conclusion we further looked at the probability of states with given energy to be found on the Mn impurities. As a result (not presented here) we found that this probability is indeed strongly increased already at the Fermi energy. It increases to almost one at even higher energies E_be close to the band edge.
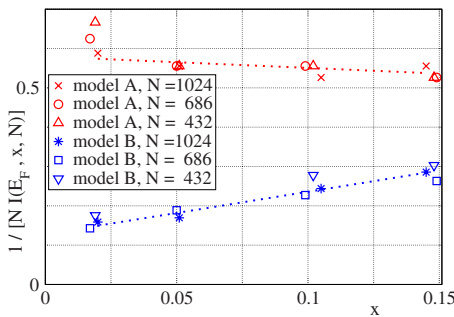

FIG. 13. (Color online) Models A and B: Scaled participation ratio $1/[N \cdot I(E_\mathrm{F},x,N)]$ at the Fermi energy as a function of the Mn concentration x. System sizes of $N=1024$, 686, and 432 atoms are shown for models A and B.
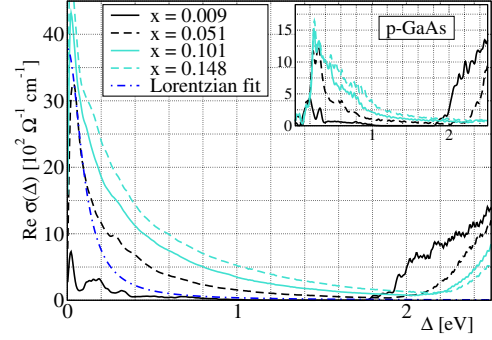

FIG. 14. (Color online) Model A: Conductivity Re $\sigma(\Delta,x)$ for various concentrations $x=0.009$ (686 atoms, $89\vec{k}$ vectors) and $x=0.051$, 0.101, and 0.148 (432 atoms, $240\vec{k}$ vectors). The results are averaged over 8 different disorder configurations. The inset shows the results for p-doped GaAs in the clean limit of the model with the corresponding number of holes added. The dashed-dotted line is a Lorentzian fit to the Drude peak at $\Delta=0$ for the $x=0.051$ data.

V. CONDUCTIVITY

The optical conductivity is a directly measurable quantity which is closely related to the absorption. As there have been various experiments studying this quantity for GaMnAs we analyze the conductivity obtainable from the two models A (Mašek) and B (Tang, Flatté) and compare our results with the experimental findings. The starting point for our analysis is the expression for the real part of the conductivity,

$$\mathrm{Re}\ \sigma(\Delta) = \frac{\pi e^2 \hbar}{m^2 \Delta} \sum_{i,f} \int_\mathrm{BZ} \frac{d^3 k}{(2\pi)^3} |\langle \Psi_{\vec{k}}^{(f)} | p_z | \Psi_{\vec{k}}^{(i)} \rangle|^2$$
$$\times \delta(E_{\vec{k}}^{(f)} - E_{\vec{k}}^{(i)} - \Delta), \tag{6}$$

where f (i) labels the final (initial) states and p_z is the z component of the momentum operator. We restrict our considerations to a linearly polarized field in z direction. As we investigate the optical conductivity in the infrared regime, the eigenstates must share the same wave vector $\vec{k}$. The resulting conductivity cannot be expected to be quantitatively exact as tight-binding approaches are known to underestimate the absorption.[42,43] Nevertheless, the order of magnitude of various related quantities, such as effective masses and important qualitative conclusions, can be extracted. Within the tight-binding approach the matrix element of the momentum operator in Eq. (6) can be expressed in terms of the Hamiltonian matrix, Eq. (3), and the distance between the localized orbitals.[44] This approximation neglects the spin-orbit coupling for the evaluation of the matrix element itself but correlations of the density of states are treated correctly giving a reasonable result for the optical conductivity.[45]

Figures 14 and 15 show the conductivity obtained from models A (Mašek) and B (Tang, Flatté), respectively. In either case, the low-frequency values are of limited accuracy as the system is of a finite size which implies a finite minimal level spacing. The minimal cutoff energy difference is set here as $\Delta_\mathrm{min} \sim 5$ meV by using a broadened δ function of this width in Eq. (6).
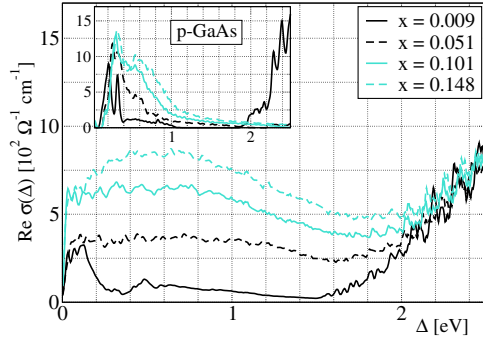
FIG. 15. (Color online) Model B: Conductivity Re $\sigma(\Delta, x)$ for various concentrations $x=0.009$ (686 atoms, 89$\vec{k}$ vectors) and x $=0.051, 0.101$, and 0.148 (432 atoms, 240$\vec{k}$ vectors). The results are averaged over 8 different disorder configurations. The inset shows the results for p-doped GaAs in the clean limit of the model with the corresponding number of holes added.

As there is a clear qualitative difference between the two models, let us start our discussion with model A (Mašek). For this model we find a low-frequency Drude peak which has also been observed in experiments.[8] For low concentrations, $x \lesssim 0.01$, additional peaks at ≈ 0.15 and ≈ 0.33 eV can be identified clearly. These additional peaks correspond to inter-valence-band transitions which blueshift to higher energy differences and become wider as the number of impurities increases. This is very similar to the experimental observations in p-doped GaAs.[46] Eventually, for concentrations $x \gtrsim 0.05$, these peaks are vanishing in the background of the Drude peak centered at $\Delta=0$. The width of this Drude peak can be related to a scattering time τ. This width and the peak height can be estimated by fitting a Lorentzian to the conductivity curve for small Δ,[8] see Fig. 14. As this fitting procedure can only be performed with some uncertainty the resulting scattering times should be considered as qualitative estimates. For the concentrations studied they range from τ ≈ 27 fs to 6 fs, see Table I. The saturation of the scattering time at high concentration is due to the break down of the independent scattering mechanism. The height of the peak gives the dc conductivity, e.g., $\sigma_{dc} \sim 4000$ Ω^{-1} cm^{-1} for x $=0.05$, which is one order of magnitude larger than the experimentally observed values.[8,9,11] Additionally the peak height and width are related to an effective mass m^*. The

TABLE I. Estimates for the dimensionless scattering length $k_F l$. The values for $(k_F l)^*$ are based on a Lorentzian fit while $(k_F l)_{opt}$ was obtained by direct integration of the numerical data. The $(k_F l)$ values for model B indicate that for the given range of parameters, the Drude-Boltzmann theory is not unambiguously applicable. We have nevertheless included the values for comparison with experimental data.

Mn concentration x	0.01	0.05	0.1	0.15
Model A: τ[fs]	27	7	6	6
Model A: $(k_F l)^*$	10	14	14	14
Model A: $(k_F l)_{opt}$	6	17	18	14
Model B: $(k_F l)_{opt}$			2.5	2.8

TABLE II. Estimates for the effective masses based on the sum rule [Eq. (7)]. The values for m^*/m_e have been obtained by the Lorentzian fit to the Drude peak obtained for model A (Mašek). The masses m_{opt}/m_e were calculated by integrating the numerical data directly.

Mn concentration x	0.01	0.05	0.1	0.15
Model A: m^*/m_e	1.0	0.5	0.9	1.0
Model A: m_{opt}/m_e	0.5	0.4	0.5	0.5
Model B: m_{opt}/m_e	0.4	0.6	0.7	0.9

estimation of this effective mass is based on a sum rule for the evaluation of the plasma frequency,

$$\omega_p^2 = \frac{2}{\pi\hbar} \int_0^{\Delta_{max}} d\Delta \text{ Re } \sigma_z(\Delta) = \frac{n_0 e^2}{m^*}, \qquad (7)$$

with n_0 being the carrier density and Δ_{max} the cutoff energy. When Eq. (7) is applied to the Lorentzian fit of the Drude peak, the cutoff energy can be set to infinity. This procedure of fitting a Lorentzian and applying the sum rule leads to effective masses $m^*/m_e \approx 0.9$, see Table II. Based on the estimates for the scattering times and these effective masses we conclude that $(k_F l)^* \approx 10-14$, see Table I, for $x=0.01-0.15$ which means that the assumption of weak scattering is applicable. However, the compensation of some of the Mn acceptors due to interstitials lowers the effective hole density and thus also decreases the values for $(k_F l)^*$ accordingly. The estimates based on experimental measurements lie between $k_F l \approx 0.75$ (Refs. 11 and 47) and $k_F l \approx 1-5$ (Refs. 8 and 14). Finally, we give an estimate of the mobility μ ≈ 13 cm^2/Vs for $x=0.1$ which is by a factor 3–5 larger than the experimental values.[8,11]

A different approach based on the sum rule is to apply Eq. (7) directly to the numerical data and choose a cutoff that includes all interband transitions but excludes valence band to conduction-band transitions,[48] i.e., $\Delta_{max}=1.5$ eV. This means that not only the narrow peak at $\Delta=0$ is considered but the wider overall shape of $\sigma(\Delta)$ which decays on an energy scale ~ 0.15 eV. This defines an optical mass m_{opt} which, for model A (Mašek), remains approximately constant, i.e., $m_{opt}/m_e \approx 0.5$, for $x=0.01-0.15$, see Table II. This is to be compared with a stronger increase in the magnitude of the optical masses $m_{opt}/m_e=0.6-1.2$ which we obtain by the same method for p-doped GaAs with the corresponding number of holes added. This discrepancy is not only in the magnitude but also in the rate of the increase in m_{opt}/m_e, with respect to the concentration x, indicates that the band structure of the host valence band is altered due to the disorder.

In strong contrast to model A (Mašek), there is no low-frequency Drude peak for model B (Tang, Flatté). For low concentrations $x=0.009$ the impurity band causes an absorption maximum around 0.1 eV. Its half-width of ~ 50 meV reflects the width of the impurity band. For higher concentrations the impurity band completely merges with the host valence band leading to a more or less constant optical absorption. This behavior is in qualitative agreement with the

experimental observations in Refs. 9 and 11. At concentrations $x \sim 0.1$ a broad feature with a maximum at 0.5 eV forms due to the larger number of impurity states which are shifted into the host gap. The absolute values of the conductivity lie between 100 and 900 Ω^{-1} cm^{-1} for the various concentrations which is in good agreement with the measurements.[8,9,11] Applying the sum rule [Eq. (7)] with $\Delta_{max} = 1.5$ eV which defines the optical mass we find $m_{opt}/m_e \approx 0.4$ for $x = 0.009$ increasing to $m_{opt}/m_e \approx 0.9$ for $x = 0.148$, see Table II. The corresponding values of p-doped GaAs range from $m_{opt}/m_e \approx 0.6$ to $m_{opt}/m_e \approx 1.2$. As we have described in Sec. IV, model B (Tang, Flatté) is close to a metal-insulator transition for the impurity concentrations considered. This is reflected by the very broad peak implying very short scattering times which are inconsistent with the weak scattering limit. For the larger concentrations $x \gtrsim 0.1$ we estimate the half-width of the broad maximum of Re $\sigma(\Delta)$ to be ~ 0.5 eV, implying $\tau \sim 1$ fs. From this follows that $\mu \sim 3$ cm^2/Vs and $k_F l \sim 2.5$ so that the mean-free path is on the order of the wavelength of the carriers. Hence the Ioffe-Regel limit is reached and a Drude-Boltzmann description of the conductivity cannot be expected to be a valid approximation any more.

In Ref. 8 the reasoning for the existence of an impurity band was based on the analysis of effective masses. However, the same analysis performed for our simulation data does not give a useful tool to distinguish the case without an impurity band from the one where an impurity band can still be identified. Although the density of states and the localization properties are very different for the two models A and B we find rather similar values for the effective and optical masses, see Table II.

VI. CONCLUSIONS

We have presented tight-binding studies of the electronic and optical properties of Ga$_{1-x}$Mn$_x$As based on two different parameterizations. The first parameterization due to Mašek (model A), is based on first-principles calculations. In this model, the Mn impurity is described by a change in the on-site and hopping terms as well as the additional inclusion of the d orbitals. This approach leads to certain qualitative changes in the electronic properties, i.e., the density of states.

However, it does not give rise to the formation of an impurity band. Instead, the inclusion of the disorder has a very similar effect as the inclusion of an equally large amount of holes without additional disorder. For the optical properties that can be deduced from Mašek's model (A), we find the formation of a Drude peak as a clear signature of the disorder. This is in agreement with recent experiments. The estimations for the dimensionless scattering length ($k_F l$) and the mobility μ give reasonable results while the absolute value of the dc conductivity is significantly larger than those observed in experiments. The interband transitions, that are also identifiable for low concentrations $x < 0.1$, blueshift with increasing amount of disorder which is in contradiction to the experiments performed on GaMnAs.

The second parameter set, by Tang and Flatté (model B), is based on a more phenomenological modeling of the Mn impurities. It describes the bound level of a single Mn impurity rather well and leads to a formation of an impurity band in the density of states of Ga$_{1-x}$Mn$_x$As for small $x \lesssim 0.01$. This impurity band merges with the host valence band at concentrations $x \sim 0.01$. The Fermi energy lies within this impurity band and the states at the Fermi level are extended for Mn concentrations between 5% and 15%. However, the eigenstates become localized for higher energies closer to the band edge. The optical conductivity is characterized by the absence of a Drude peak at zero frequency and a rather featureless shape. It shows a broad maximum for larger Mn concentrations with a half-width of approximately 0.5 eV. From this width we deduce short scattering times leading to the conclusion that a Drude-Boltzmann theory of weak scattering is not applicable.

As the experiments on the electronic properties of GaMnAs are not entirely conclusive at the moment, it is difficult to judge which model fits best for a given physical quantity. Either model describes some of the experimental findings correctly while it fails for others.

*marko.turek@physik.uni-regensburg.de

[1] H. Ohno, Science **281**, 951 (1998).

[2] T. Jungwirth, J. Sinova, J. Mašek, J. Kucera, and A. H. MacDonald, Rev. Mod. Phys. **78**, 809 (2006).

[3] J. Fabian, A. Matos-Abiague, C. Ertler, P. Stano, and I. Žutic, Acta Phys. Slov. **57**, 565 (2007).

[4] T. Dietl, J. Appl. Phys. **103**, 07D111 (2008).

[5] T. Jungwirth et al., Phys. Rev. B **72**, 165204 (2005).

[6] A. H. MacDonald, P. Schiffer, and N. Samarth, Nat. Mater. **4**, 195 (2005).

[7] M. Linnarsson, E. Janzén, B. Monemar, M. Kleverman, and A. Thilderkvist, Phys. Rev. B **55**, 6938 (1997).

[8] K. S. Burch, D. B. Shrekenhamer, E. J. Singley, J. Stephens, B. L. Sheu, R. K. Kawakami, P. Schiffer, N. Samarth, D. D. Awschalom, and D. N. Basov, Phys. Rev. Lett. **97**, 087208 (2006).

[9] S. Katsumoto et al., Mater. Sci. Eng., B **84**, 88 (2001).

[10] Y. Nagai, T. Kunimoto, K. Nagasaka, H. Nojiri, M. Motokawa, F. Matsukura, T. Dietl, and H. Ohno, Jpn. J. Appl. Phys., Part 1 **40**, 6231 (2001).

[11] K. Hirakawa, S. Katsumoto, T. Hayashi, Y. Hashimoto, and Y. Iye, Phys. Rev. B **65**, 193312 (2002).

[12] T. Tsuruoka, N. Tachikawa, S. Ushioda, F. Matsukura, K. Takamura, and H. Ohno, Appl. Phys. Lett. **81**, 2800 (2002).

[13] O. Thomas, O. Makarovsky, A. Patanè, L. Eaves, R. P. Campion,

K. W. Edmonds, C. T. Foxon, and B. L. Gallagher, Appl. Phys. Lett. **90**, 082106 (2007).

[14] T. Jungwirth *et al.*, Phys. Rev. B **76**, 125206 (2007).

[15] L. M. Sandratskii, P. Bruno, and J. Kudrnovský, Phys. Rev. B **69**, 195203 (2004).

[16] A. Stroppa, S. Picozzi, A. Continenza, M. Y. Kim, and A. J. Freeman, Phys. Rev. B **77**, 035208 (2008).

[17] J.-M. Tang and M. E. Flatté, Phys. Rev. Lett. **92**, 047201 (2004).

[18] P. VanDorpe, W. VanRoy, J. DeBoeck, G. Borghs, P. Sankowski, P. Kacman, J. A. Majewski, and T. Dietl, Phys. Rev. B **72**, 205322 (2005).

[19] P. Sankowski, P. Kacman, J. Majewski, and T. Dietl, Physica E (Amsterdam) **32**, 375 (2006).

[20] J. Mašek, J. Kudrnovský, F. Máca, J. Sinova, A. H. MacDonald, R. P. Campion, B. L. Gallagher, and T. Jungwirth, Phys. Rev. B **75**, 045202 (2007).

[21] R. Bhatt, M. Berciu, M. P. Kennett, and X. Wan, J. Supercond. **15**, 71 (2002).

[22] A. Kaminski and S. DasSarma, Phys. Rev. Lett. **88**, 247202 (2002).

[23] S. DasSarma, E. H. Hwang, and A. Kaminski, Phys. Rev. B **67**, 155201 (2003).

[24] M. A. Majidi, J. Moreno, M. Jarrell, R. S. Fishman, and K. Aryanpour, Phys. Rev. B **74**, 115205 (2006).

[25] T. Dietl, H. Ohno, F. Matsukura, J. Cibert, and D. Ferrand, Science **287**, 1019 (2000).

[26] T. Dietl, H. Ohno, and F. Matsukura, Phys. Rev. B **63**, 195205 (2001).

[27] S. R. Eric Yang, J. Sinova, T. Jungwirth, Y. P. Shim, and A. H. MacDonald, Phys. Rev. B **67**, 045205 (2003).

[28] M. Elsen, H. Jaffres, R. Mattana, M. Tran, J.-M. George, A. Miard, and A. Lemaitre, Phys. Rev. Lett. **99**, 127203 (2007).

[29] Y. Yildirim, G. Alvarez, A. Moreo, and E. Dagotto, Phys. Rev.

Lett. **99**, 057207 (2007).

[30] D. J. Chadi, Phys. Rev. B **16**, 790 (1977).

[31] D. N. Talwar and C. S. Ting, Phys. Rev. B **25**, 2660 (1982).

[32] J. Mašek (private communication).

[33] D. Kitchen, A. Richardella, J.-M. Tang, M. Flatté, and A. Yazdani, Nature (London) **442**, 436 (2006).

[34] T. Dietl, J. Phys. Soc. Jpn. **77**, 031005 (2008).

[35] J. Slater and G. Koster, Phys. Rev. **94**, 1498 (1954).

[36] W. Harrison, *Elementary Electronic Structure* (World Scientific, Singapore, 1999).

[37] G. Lehmann and M. Tauc, Phys. Status Solidi B **54**, 469 (1972).

[38] J. Okabayashi, A. Kimura, O. Rader, T. Mizokawa, A. Fujimori, T. Hayashi, and M. Tanaka, Physica E (Amsterdam) **10**, 192 (2001).

[39] J. Okabayashi, A. Kimura, O. Rader, T. Mizokawa, A. Fujimori, T. Hayashi, and M. Tanaka, Phys. Rev. B **58**, R4211 (1998).

[40] J. S. Blakemore, J. Winfield, J. Brown, M. L. Stass, and D. A. Woodbury, J. Appl. Phys. **44**, 3352 (1973).

[41] S. Sanvito and N. A. Hill, Phys. Rev. B **62**, 15553 (2000).

[42] S.-Y. Ren and W. A. Harrison, Phys. Rev. B **23**, 762 (1981).

[43] J.-M. Jancu, R. Scholz, F. Beltram, and F. Bassani, Phys. Rev. B **57**, 6493 (1998).

[44] G. Theodorou and G. Tsegas, Phys. Status Solidi B **211**, 847 (1999).

[45] L. C. Lew Yan Voon and L. R. Ram-Mohan, Phys. Rev. B **47**, 15500 (1993).

[46] W. Songprakob, R. Zallen, D. Tsu, and W. Liu, J. Appl. Phys. **91**, 171 (2002).

[47] K. Wagner, D. Neumaier, M. Reinwald, W. Wegscheider, and D. Weiss, Phys. Rev. Lett. **97**, 056803 (2006).

[48] J. Sinova, T. Jungwirth, S. R. Eric Yang, J. Kučera, and A. H. MacDonald, Phys. Rev. B **66**, 041202(R) (2002).